ENGINEERING

Magnetic kirigami dome metasheet with high deformability and stiffness for adaptive dynamic shape-shifting and multimodal manipulation

Yinding Chi[1], Emily E. Evans[2], Matthew R. Clary[3], Fangjie Qi[1], Haoze Sun[1], Saarah Niesha Cantú[3], Catherine M. Capodanno[2], Joseph B. Tracy[3]*, Jie Yin[1]*

Soft shape-shifting materials offer enhanced adaptability in shape-governed properties and functionalities. However, once morphed, they struggle to reprogram their shapes and simultaneously bear loads for fulfilling multifunctionalities. Here, we report a dynamic spatiotemporal shape-shifting kirigami dome metasheet with high deformability and stiffness that responds rapidly to dynamically changing magnetic fields. The magnetic kirigami dome exhibits over twice higher doming height and 1.5 times larger bending curvature, as well as sevenfold enhanced structural stiffness compared to its continuous counterpart without cuts. The metasheet achieves omnidirectional doming and multimodal translational and rotational wave-like shape-shifting, quickly responding to changing magnetic fields within 2 milliseconds. Using the dynamic shape-shifting and adaptive interactions with objects, we demonstrate its applications in voxelated dynamic displays and remote magnetic multimodal directional and rotary manipulation of nonmagnetic objects without grasping. It shows high-load transportation ability of over 40 times its own weight, as well as versatility in handling objects of different materials (liquid and solid), sizes, shapes, and weights.

INTRODUCTION

Shape-shifting matter is intriguing in nature and engineering (*1*–*4*). Shape changes modify both properties and functionalities of materials for broad applications in adaptive structures, medical devices, wearable electronics, and soft robotics (*4*–*8*). For example, a thin two-dimensional (2D) sheet may morph into complex 3D surfaces with programmable nonzero Gaussian curvature (*3*, *9*). This transformation can be achieved by programming composite patterns, inducing inhomogeneous swelling or expansion in active materials in response to external environmental stimuli, or by designing specific folding or cutting patterns in origami and kirigami structures (*10*). For example, a thin sheet can morph into dome or saddle shapes through anisotropic in-plane or cross-thickness swelling in hydrogels, triggered by changes in temperature, light, pH, or electric field (*3*). Similar shape morphing can also be achieved by stretching a kirigami sheet with patterned cuts (*11*, *12*). However, once morphed, reprogramming and dynamically shifting these shapes without altering the prescribed swelling or cut patterns remains challenging (*10*–*12*). In addition, there is a contradiction in soft shape-shifting materials between the need for high structural compliance, which facilitates deformability and shape adaptivity to dynamically changing stimuli, and the requirement for high stiffness, which enables load-carrying capacities during and after morphing to fulfill multifunctionality (*3*).

To tackle the challenges in soft shape-morphing materials with both shape reprogrammability and high stiffness, recent research has introduced a sandwiched soft-hard composite lattice-based robotic surface for reprogrammable shape morphing and object manipulation (*8*). The shape morphing is actuated using heat-responsive liquid crystal elastomers (LCEs) via Joule heating. The thermal actuation in the top and bottom soft LCE layers drives the buckling of the hard polymer ribbon networks sandwiched between them, enabling both shape transformation and load-bearing capabilities. However, despite these advancements, the system requires a stiff ribbon network to substantially enhance the stiffness in LCEs for load supports, as well as multiple control channels that are tethered to power systems (*8*), complicating the control for morphing and manipulation.

Among environmental stimuli, magnetic fields provide a promising solution for dynamic shape morphing in soft materials (*13*–*15*) because they are remote, have a fast response, and are easily controllable. Despite these capabilities, challenges in reprogramming dynamic shape-shifting and resolving the contradiction between high deformability and stiffness remain to be addressed in soft magnetic morphing materials. There has been minimal exploration concerning how to reprogram controllable spatiotemporal dynamic shape-shifting and propagation across magnetoresponsive thin sheets under dynamically changing magnetic fields (*13*, *16*, *17*), as well as how to leverage it for stiffness modulation and functionalities (*18*, *19*).

Here, we report combining cut-induced flexibility and shape adaptivity in domes to create a dynamically shape-shifting and stiffening magnetic kirigami dome metasheet. A flat thin sheet with programmed ferromagnetic domains transforms into a metasheet with a periodic array of domes under static magnetic fields. Compared to the continuous magnetic dome metasheet without cuts, the kirigami design allows for a doming height nearly twice as high, despite having an over fivefold lower modulus (*20*–*22*), while achieving nearly double the structural stiffness for over fourfold load-bearing and load-lifting capacities. The achieved high deformability and stiffness enable a large working space and high actuation force, facilitating multifunctionality in adaptive dynamic shape-shifting and object manipulation. Beyond simple pop-up or down shape morphing in bistable continuous domes (*23*, *24*), the

[1]Department of Mechanical and Aerospace Engineering, North Carolina State University, Raleigh, NC 27695, USA. [2]Department of Physics and Astronomy, Elon University, Elon, NC 27244, USA. [3]Department of Materials Science and Engineering, North Carolina State University, Raleigh, NC 27695, USA.
*Corresponding author. Email: jbtracy@ncsu.edu (J.B.T.); jyin8@ncsu.edu (J.Y.)

magnetic kirigami dome metasheet enables dynamic omnidirectional doming in individual domes and collective translational and rotational wave-like shape-shifting across the sheet under changing magnetic fields. Numerical simulation based on simplified theoretical modeling is developed to predict these dynamic doming shape changes. By leveraging the adaptive and dynamic interactions between the shape-shifting metasheet and objects on top, we demonstrate its applications in multimodal remote magnetic manipulation of various nonmagnetic solid and liquid objects without grasping.

RESULTS

Magnetic kirigami dome with high deformability

Figure 1 (A to C) illustrates the fabrication and actuation of a single magnetic kirigami dome and its continuous counterpart without cuts for comparison through four steps: air inflation, magnetization, deflation, and magnetic actuation (see Materials and Methods for details). The process begins with an unmagnetized kirigami or continuous disk made of magnetoresponsive elastomers (~265 μm in thickness and 5 mm in radius; see fig. S1 for microscale features and magnetic properties). The kirigami disk is patterned with orthogonal square cuts (cut length $L = 1.5$ mm and cut width $d = 250$ μm; cut ratio $L/d = 6$) via laser cutting (inset of Fig. 1A) (*20*, *21*). The disk is placed on an inflatable elastomeric membrane (80 μm in thickness), and then pneumatic pressure P is applied by inflating a small air volume (<1 ml). Both kirigami and uncut disks conform to the elastomeric balloon, forming a porous dome and a continuous dome, respectively (Fig. 1B, i; fig. S2, A and B; and movie S1).

The inflated doming height h_p can be tuned by P and the cut ratio L/d; increasing either parameter results in a higher dome (fig. S2, C and D) due to reduced stiffness at a larger L/d (fig. S3). The inflated dome is then magnetized under uniform magnetizing field with an intensity of $M = 1.23$ T (Fig. 1B, i) in the out-of-plane direction (i.e., z axis). After deflation, both magnetized domes return to a flat state with a preserved local periodic magnetization profile $\boldsymbol{M}$ (fig. S4A). Applying a uniform magnetic field $\boldsymbol{B}$ along the vertical direction (z axis) generates a spherical dome shape but with over 1.7 times smaller doming height than h_p (Fig. 1C and fig. S2C).

The kirigami design enhances flexibility and deformability compared to its continuous counterpart without cuts. The unmagnetized kirigami disk achieves a much higher doming height h_p than the continuous one under the same pressure P, e.g., at $P = 33$ kPa, h_p ~7 mm in the kirigami dome, nearly 1.75 times higher than the continuous dome (h_p ~4 mm; Fig. 1B and fig. S2C). Similarly, the magnetized kirigami disk also shows a much higher doming height h_B and larger bending curvature under the same magnetic field B

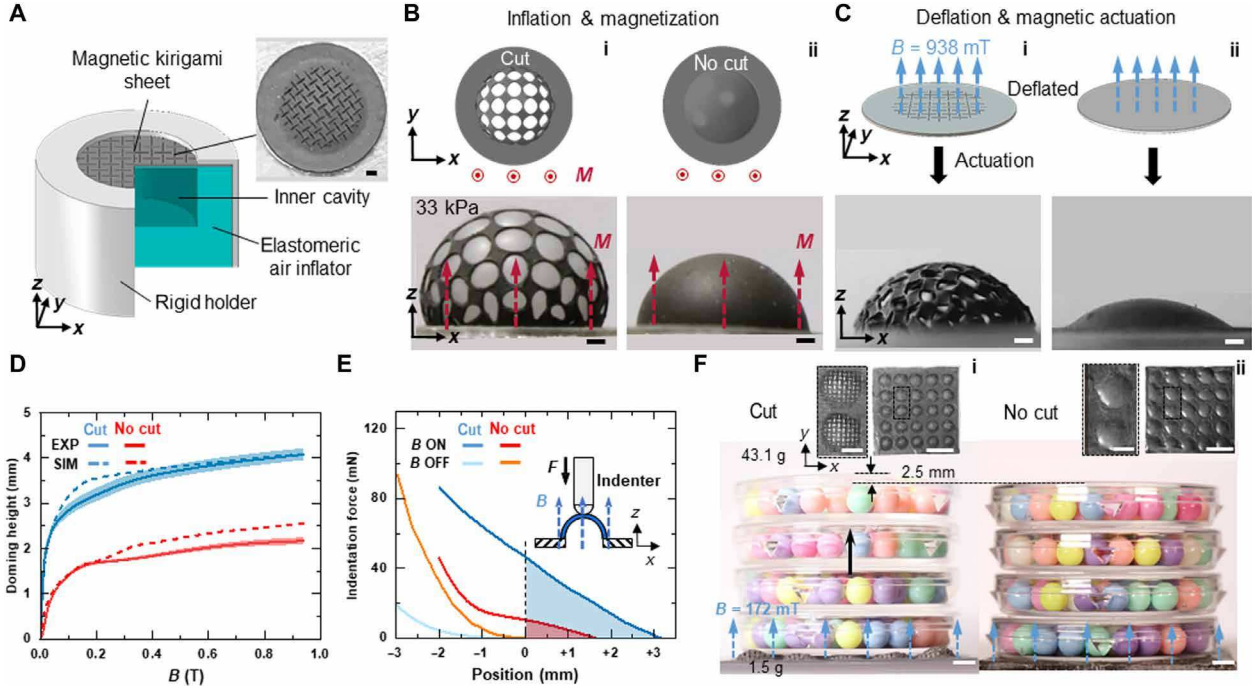

Fig. 1. Magnetic kirigami dome with high deformability and stiffness. (**A**) Schematic setup of inflating a magnetic kirigami disk with patterned orthogonal cuts into a dome shape under an air pressure P. The inset shows the photo of the magnetic kirigami disk. Scale bar, 1.5 mm. (**B**) Top view (schematics, xy plane) and front views (photos, xz plane) of the inflated magnetic kirigami dome (i) and its counterpart, a continuous dome without cuts (ii), under the same inflation pressure $P = 33$ kPa, followed by magnetization under the same uniform field intensity of $M \sim 1.23$ T along the z axis. Scale bars, 1.5 mm. (**C**) Photos (front view, xz plane) of the vertically actuated kirigami dome (i) and continuous dome (ii) under the same applied magnetic field $B = 938$ mT along the z axis as schematically illustrated on the top row. Scale bars, 1.5 mm. (**D**) Experimental and theoretical results on the comparison of the actuated dome height h_B as a function of B between a single magnetic kirigami dome and its continuous counterpart without cuts under the same inflation and magnetization states. (**E**) Comparison of the indentation force and position (f-p) curves of a single magnetic dome with/without cuts when the applied magnetic field B is on and off. The inset shows the schematic experimental setup for the indentation test under the same vertical magnetic field ($B = 152$ mT). (**F**) Demonstration of high load-lifting and bearing capability of the 5 by 5 magnetic kirigami dome metasheet (i). The metasheet (1.5 g) can lift a weight of 43.1 g at a height of 2.5 mm under an applied $B = 172$ mT. The magnetic continuous dome metasheet remains flat and fails to lift the same object under the same magnetic field (ii). Scale bars, 5 mm. EXP, experiment; SIM, simulation.

(Fig. 1C). Figure 1D shows that, as B increases, h_B first rises markedly and then plateaus for both kirigami and continuous domes (fig. S5, A and B). The plateaued h_B at $B = 938$ mT for the kirigami dome is $h_B \sim 4.1$ mm, which is over twice as high as the continuous dome. This notable increase in doming height for the kirigami disk is attributed to the cut-induced marked reduction in its Young's modulus E (*21*), where E in the kirigami sheet (~37.5 kPa for $L/d = 6$) is over 5.5 times lower than that of the continuous sheet (fig. S3B). Furthermore, compared to continuous disks, the cuts introduce an additional degree of freedom in rotation (Fig. 1, B and C, i) (*20*–*22*). This rotational flexibility allows the discrete cut panels to stretch and bend more easily during both processes of pneumatic inflation and external magnetic field actuation, whereas such rotational deformation is largely restricted in the continuous structure (Fig. 1B). In addition, these rotations complicate the local magnetization orientations in the deformed cut panels during inflation, which are preserved as the panels rotate back to their original positions (fig. S4A and more discussions in the Supplementary Materials). This results in more intricate interactions between the cut panels and the external magnetic fields. The increased rotational freedom not only enhances flexibility in shape morphing but also, along with the higher doming height, provides a larger working space for multifunctional capabilities in potential dynamic shape transformation and object manipulation under spatiotemporal magnetic fields, as discussed later.

Magnetic stiffening of the kirigami dome

In addition to its high flexibility and deformability, the kirigami dome also shows high stiffness under magnetic actuation. Typically, there is a contradiction between compliance and load-bearing capacity in kirigami structures due to cut-induced stiffness reduction (*21*, *25*). We explore magnetic-induced stiffness modulation (*18*) as a method to overcome this limitation in the kirigami dome.

An indentation test was conducted to evaluate the stiffening effect in both kirigami and continuous samples when an external vertical magnetic field B was applied and removed (Fig. 1E and fig. S6). The experimental setup is illustrated in the inset of Fig. 1E (see fig. S6A and Materials and Methods for details). Under the same magnetic field ($B = 152$ mT), the kirigami dome reaches a height h_B of about 3.2 mm, double that of the continuous dome ($h_B \sim 1.6$ mm). When the magnetic field is turned off, both domes return to their flat disk shape. Figure 1E shows four indentation force-position (f-p) curves for the kirigami and continuous domes with the magnetic field on and off. The position p is measured positively from the base at $z = 0$, starting from $p_o = h_B$ for both domes and from $p_o = 0$ for both flat disks, where $f = 0$. The indentation force f in both domes increases almost linearly as the position p decreases ($p > 0$) or equivalently as the indentation displacement d increases (fig. S6B, ii), where $d = p_o - p$. Compared to the continuous dome, the kirigami dome shows a notably higher indentation force and results in eight times more work done at positive displacements (highlighted in shaded areas with 69 μN·m versus 8.2 μN·m; Fig. 1E). Thus, the kirigami dome can potentially maximize the work done in lifting an object. As p approaches zero, the dome reaches a nearly flattened state, and the corresponding indentation force $f_{p=0}$ at $p = 0$ (dashed line in Fig. 1E) can be approximately considered the maximum load capacity of the structure. At $p = 0$, $f_{p=0}$ is about 46.7 mN in the kirigami dome, more than 4.5 times higher than in the continuous dome, highlighting the cut-induced enhancement in the load-bearing capacity of the magnetic kirigami dome. When the magnetic field is off, both domes, now flat disks, exhibit a highly nonlinear force-position (f-p) and force-displacement (f-d) curve (fig. S6B).

To quantify the effect of the magnetic field and kirigami design on stiffness modulation, we evaluated the effective structural stiffness K as the initial slope of the f-d curves (fig. S6, B and C). As the applied magnetic field B increases from 0 to 152 mT, the stiffness increases by 23 times in the kirigami dome and 3 times in the continuous dome (fig. S6, B and C, and table S1), indicating substantial magnetically induced stiffening. Under the same $B = 152$ mT, the kirigami dome shows over 1.8 times the stiffness (K~13.8 N/m) compared to the continuous dome. However, this result contradicts theoretical predictions, which suggest that the kirigami dome should have lower stiffness due to cut-induced material compliance. Theoretical models indicate that structural stiffness K in an elastic spherical shell scales with (*26*)

$$K \propto \frac{Et^2}{R} \tag{1}$$

where E is the Young's modulus, t is the shell thickness, and R is the shell radius. Given the kirigami dome's over 5.5 times lower Young's modulus ($E_{\text{uncut}} = 209$ kPa and $E_{\text{kirigami}} = 37.45$ kPa; $L/d = 6$) and 1.5 times smaller bending radius (Fig. 1C and fig. S3B), from Eq. 1, the continuous dome is theoretically predicted to have approximately four times higher stiffness. The large discrepancy between experimental results and theoretical expectations can be attributed to the interactions between the kirigami structure and the external magnetic field, which are not considered in the theoretical model. Thus, this suggests a sevenfold enhancement in stiffening in the kirigami dome, driven by the combined effects of the applied magnetic field and the kirigami design.

For the magnetic kirigami dome, its doming height h_B, stiffness K, and load capacity $f_{p=0}$ can be further manipulated by tuning the magnetizing fields with different intensities M (fig. S6D) and the cut ratio L/d of the kirigami pattern (fig. S6E). As M increases from 1.03 to 1.23 T, h_B rises modestly by 22%, K increases by 57%, and $f_{p=0}$ markedly increases by 118%. Further increasing M from 1.23 to 1.41 T results in a negligible increase (2.5%) in doming height and a slight increase (~25%) in both stiffness and load capacity (fig. S6D and table S1). When the cut ratio L/d increases from 4 to 12, despite a notable 5.5-fold reduction in Young's modulus (fig. S3B and table S1), h_B only increases slightly by 19% to 3.4 mm (fig. S6E and table S1), due to the stiffening effect caused by the transition from rotational to stretching deformation in the cut panels (fig. S2D) (*22*). In contrast, K and $f_{p=0}$ do not exhibit a monotonic decrease with increasing L/d but show peak values of $K_{\max} = 13.8$ N/m and $(f_{p=0})_{\max} = 46.2$ mN at an intermediate $L/d = 6$. This is expected as, at $L/d = 12$, the kirigami dome becomes too compliant to support certain loads despite the magnetic stiffening effect. At this ratio, the Young's modulus of the kirigami sheet is reduced by nearly 15 times compared to the thin sheet without cuts (table S1). This suggests an optimal design that overcomes the typical trade-off between compliance (high deformability) and stiffness (load-bearing capacity) in shape-morphing structures, where a higher L/d in kirigami domes typically results in greater doming height but lower stiffness due to the reduced modulus. For example, at $L/d = 12$ versus $L/d = 4$, we observe $h_B = 3.4$ mm versus 2.8 mm, $K = 6.1$ N/m versus 12.1 N/m, and $E = 14.3$ kPa versus 77.2 kPa (table S1). Thus, the kirigami dome with an optimal cut ratio of $L/d = 6$,

which balances high deformability and stiffness, is selected for further exploration of its multifunctionality.

Building on the stiffening effect observed in kirigami domes, we further demonstrate that the kirigami design enhances the load-lifting capability in a dome metasheet. This metasheet is composed of a 5 by 5 array of domes (inset of Fig. 1F, i), fabricated using a process similar to that of a single dome (see fig. S7 and Materials and Methods for details). Despite its inherent compliance, the kirigami dome metasheet exhibits high load-lifting capabilities under magnetic actuation. It successfully lifts a weight of 43.1 g, which is 28 times its own weight (1.5 g), and holds it at a height of 2.5 mm under an applied magnetic field of $B = 172$ mT (Fig. 1F, i and movie S2). In contrast, the continuous dome metasheet (inset of Fig. 1F, ii) remains flat under the same magnetic field, unable to lift the same weight (Fig. 1F, ii and movie S3).

Omnidirectional doming and simplified modeling

The kirigami structure enables omnidirectional doming when magnetic actuated by tuning the angle α between the disk's normal direction $\boldsymbol{n}$ of its top surface and the applied magnetic field $\boldsymbol{B}$ (Fig. 2A and fig. S5, B to F). α is positive when measured clockwise (cw) from $\boldsymbol{n}$ to $\boldsymbol{B}$. As α increases from 0° to 180°, the dome becomes asymmetrical and the height gradually decreases at α = 50° (Fig. 2A, i and ii and fig. S5C), followed by a slightly concave shape at α = 90° (fig. S5D), and an inverted sharp conical dome at α = 180° (Fig. 2A, iii and fig. S5E). Negative α values, such as α = −130°, result in a conical droplet shape (Fig. 2A, iv and fig. S5F). The conical shapes in Fig. 2A, iii and iv are due to the combined effects of magnetic and gravitational forces.

Numerical simulations based on simplified theoretical modeling were conducted to better understand shape-shifting in the kirigami dome under magnetic fields of varying magnitudes and directions (see Materials and Methods and the Supplementary Materials). As a simplification, the dome is modeled in cross section, as a 1D strip of a continuous, elastic, and homogeneous magnetic sheet (Fig. 2B). The simulation mirrors the experimental procedures (Fig. 1, B and C). In a typical simulation, an unmagnetized strip is inflated by applied pressure, causing it to stretch and bend. The inflated strip is then magnetized in the vertical direction (Fig. 2C, i), with the local magnetization orientation preserved as the pressure is released, allowing the strip to relax back to a flat state (Fig. 2C, ii). Last, a uniform magnetic field $\boldsymbol{B}$ is applied with the

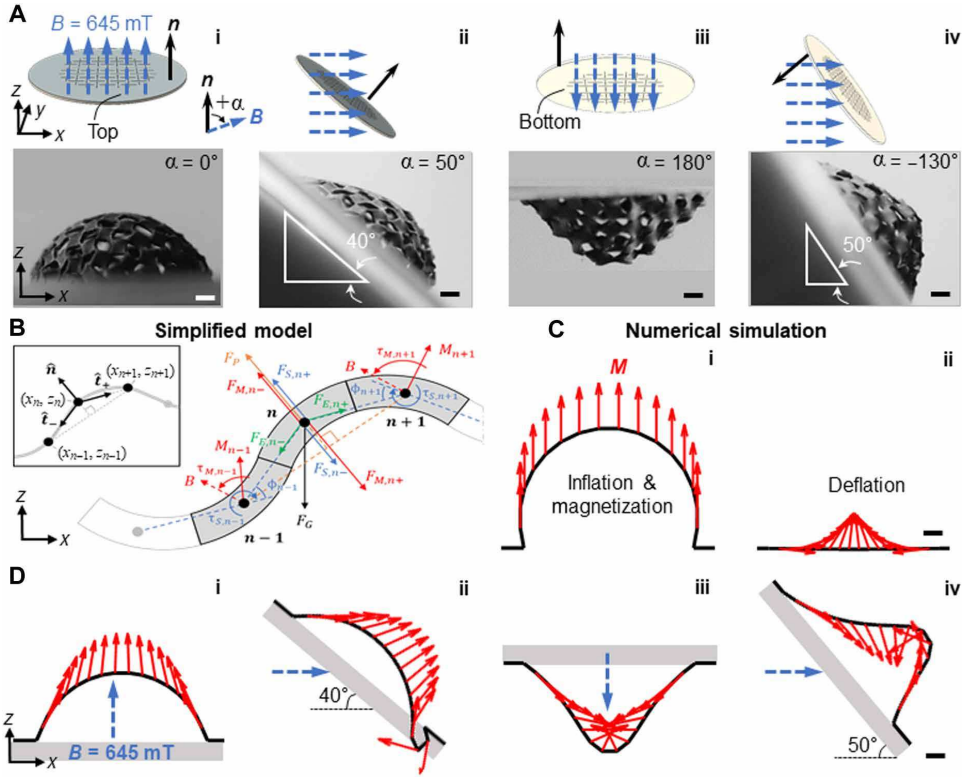

Fig. 2. Omnidirectional doming in the magnetic kirigami dome under varying directional magnetic field. (**A**) Photos (front view, *xz* plane) of the directionally actuated kirigami dome under the same $B = 645$ mT but with different angles of α = 50° (i), 50° (ii), 180° (iii), and −130° (iv), as illustrated on the top row. The angle between the applied $\boldsymbol{B}$ and the disk's normal direction $\boldsymbol{n}$ is denoted as α. Scale bars, 1.5 mm. (**B**) Schematic illustration of the simplified magnetic kirigami strip model composed of discrete segments and vertices. It shows the free-body diagram of a representative segment with the five forces labeled, including gravitational force F_G acting downward (black), pneumatic pressure F_P applied normally to the strip (orange), elastic extension (compression) forces $F_{E,n\pm}$ (green), restoring bending forces $F_{S,n\pm}$ normal to the strip (blue), and magnetic forces $F_{M,n\pm}$ from the magnetic torques (red). A viscous fluid force (not shown) acts opposite the velocity of each segment to dampen motion as the film relaxes toward equilibrium. Inset: Definitions of normal $(\hat{n})$ and tangent $(\hat{t}_-, \hat{t}_+)$ unit vectors used in force calculations. (**C**) Simulation results on inflation and magnetization, followed by deflation processes. The red arrows denote the magnetization profile *M*. Scale bar, 1.5 mm. (**D**) Theoretically predicted actuated cross-sectional kirigami dome shapes under the same $B = 645$ mT but with different angles of α = 0° (i), 40° (ii), 180° (iii), and −130° (iv). Scale bar, 1.5 mm. The blue arrows denote the direction of the external magnetic field.

specified magnitude and direction, and the new configuration of the strip is determined (Fig. 2D).

The strip is modeled as a series of discrete vertices (Fig. 2B), where each vertex represents a segment of the strip, with its 2D coordinates denoted as (x_n, y_n) for $1 \le n \le p$, where p is the total number of segments (inset of Fig. 2B). Figure 2B highlights three neighboring segments and their associated vertices as examples. Each vertex, except for the two end vertices, experiences five forces: gravitational, elastic stretching (or compression), elastic bending, magnetic torque, and any applied pneumatic pressure (Fig. 2B).The gravitational force $\vec{F}_{G,n}$ is proportional to the mass of each segment, m_n, and can be specified at an angle θ_G from the vertical

$$\vec{F}_{G,n} = m_n g \langle \sin\theta_G, \cos\theta_G \rangle \quad (2)$$

This force is independent of the location of the other vertices. However, for other forces, it is necessary to account for the relative locations of neighboring vertices by calculating three directional vectors, including a unit vector normal to the surface, $\hat{\boldsymbol{n}}$, and unit tangent vectors, $\hat{\boldsymbol{t}}_+$ and $\hat{\boldsymbol{t}}_-$, indicating directions toward the neighboring $n+1$ and $n-1$ vertices, respectively (Fig. 2B, inset). Following this, elastic extension (compression) forces $\vec{F}_{E,n\pm}$ between vertices are given by

$$\vec{F}_{E,n\pm} = Ewt\frac{L_{n\pm} - L}{L}\hat{\boldsymbol{t}}_{\pm} \quad (3)$$

where w and t are the strip's width and thickness, respectively. $L_{n\pm}$ is the distance between the nth and $(n\pm1)$th vertices, and L is the relaxed length of a segment. As the strip bends, restoring forces arise due to elastic bending. This is modeled as a thin beam bent through a constant curvature between successive vertices, for which the restoring bending moment $\tau_{S,n\pm1}$ is given by $\tau_{S,n\pm1} = \frac{Ewt^3}{3L}\phi_{n\pm1}$ (*27*), where $\phi_{n\pm1}$ is the relative bending angle. The resulting forces $\vec{F}_{S,n\pm}$ on vertex n due to bending at the $n \pm 1$ vertices are then given by

$$\vec{F}_{S,n\pm} = \mp L^{-1}\tau_{S,n\pm1}\hat{\boldsymbol{n}} = \mp\frac{Ewt^3}{3L^2}\phi_{n\pm1}\hat{\boldsymbol{n}} \quad (4)$$

Magnetic torques are calculated similarly, with magnetic torques on the $n \pm 1$ vertices depending on the cross product of the local magnetization $\vec{\boldsymbol{M}}_{n\pm1}$ and the applied field $\vec{\boldsymbol{B}}$, i.e., $\vec{\tau}_{M,n\pm1} = wLt\vec{\boldsymbol{M}}_{n\pm1} \times \vec{\boldsymbol{B}}$, resulting in the magnetic forces on the nth vertex of

$$\vec{F}_{M,n\pm} = \mp L^{-1}\tau_{M,n\pm1}\hat{\boldsymbol{n}} = \mp wt\,\mathrm{sgn}(\vec{\boldsymbol{M}}_{n\pm1} \times \vec{\boldsymbol{B}})\left|\vec{\boldsymbol{M}}_{n\pm1} \times \vec{\boldsymbol{B}}\right|\hat{\boldsymbol{n}} \quad (5)$$

The force due to pneumatic pressure P is given by

$$\vec{F}_P = PLw\,\hat{\boldsymbol{n}} \quad (6)$$

A nonconservative viscous drag force is also included to dissipate energy (see the Supplementary Materials for details). To find the equilibrium configuration, the net force on each vertex is calculated, and the strip accelerates over a small time step Δt, after which forces are reassessed. This process is repeated until the sum of the magnitudes of the net force on each segment falls below a threshold (0.1 μN), ensuring that the strip reaches a minimum-energy state. The direction and magnitude of $\vec{\boldsymbol{B}}$ can be adjusted to simulate the strip's response to time-varying magnetic fields, such as those produced by an array of magnets.

In this work, the simulation well captures the variation of doming height with increasing $\boldsymbol{B}$ with $\alpha = 0°$ (Fig. 1D) and the shape-shifting from round to sharp conical shapes at different values (Fig. 2D) observed in the experiment (Fig. 2A).

Spatiotemporal fast-response dynamic shape-shifting in the metasheet

Next, we explore the spatiotemporal dynamic shape-shifting and propagation in the kirigami dome metasheet driven by the dynamically moving and rotating magnetic fields underneath controlled by linear and rotational motors (Materials and Methods and fig. S8). The dome metasheet (5 by 5) is fixed onto a rigid holder by bonding its uncut boundaries to counter the pulling magnetic force induced by the magnetic gradient (Fig. 3A). Figure 3 (B to D) shows the schematic setups for exploring how the shape-shifting dome metasheet on top responds to the local and global out-of-plane dynamically changing magnetic fields $\boldsymbol{B}$, including a moving letter "C"-like pattern of localized pillar magnets (Fig. 3B), a moving array of nine bar-shaped magnets with alternate orientations (Fig. 3C), and a spinning capsule-shaped magnet (Fig. 3D). The simplified model is also used to simulate the quasistatic wave-like behavior by applying a sequence of field values (magnitude and direction) deduced from finite element analysis simulations of permanent magnets (Fig. 3E; see more details in the Supplementary Materials).

For these different configurations of magnets, a single dome in the metasheet shows a similar shape-shifting response to a dynamic magnetic field $\boldsymbol{B}$ with both dynamically changing magnitude and direction. As an example, Fig. 3E shows the simulation results on the periodic dynamic shape-shifting in a dome in response to a right-moving magnetic field in Fig. 3C (see more details on other results in response to magnetic motions in Fig. 3, B and D; fig. S8A; and movie S4). As the array of bar-shaped magnets moves to the right, $\boldsymbol{B}$ starts to rotate counterclockwise (ccw) with spatiotemporal magnitude and angle changes. The rotating angle α is defined as positive when rotating cw from the positive z axis (inset of Fig. 3E). Because the omnidirectional doming in the kirigami dome aligns with the changing directions of $\boldsymbol{B}$, as $\boldsymbol{B}$ rotates ccw starting from 0° to complete a full circle, the upward round doming shifts into a downward conical dome ($\beta \sim -180°$) passing through intermediate asymmetric doming (Fig. 3E, i to v), e.g., asymmetric S and droplet shapes. As $\boldsymbol{B}$ continues rotating ccw back with reduced magnitude, the metasheet undergoes a reverse shape-shifting process but with mirrored shapes about the z axis and smaller doming height (Fig. 3E, vi to ix). Repeating such shape-shifting in the array of the domes with a phase angle shifting related to the moving or spinning speed of magnets generates a translational or rotational wave propagation–like motion in the metasheet shown in Fig. 4 and fig. S9.

Figure 4 shows the corresponding time-lapse top-view images of the shape-shifting metasheets over one time period β when the magnets move from left to right or complete a full spin (movie S5). Figure 4A shows that, as the patterned C-shaped magnets move to the right, the localized domes sequentially pop up and return to flat, acting as dynamic voxels for physically displaying a scrolling letter "C" in the metasheet. When the metasheet is sequentially actuated column by column by the moving bar-shaped magnets, it generates continuous dynamic wave propagation to the right with alternating

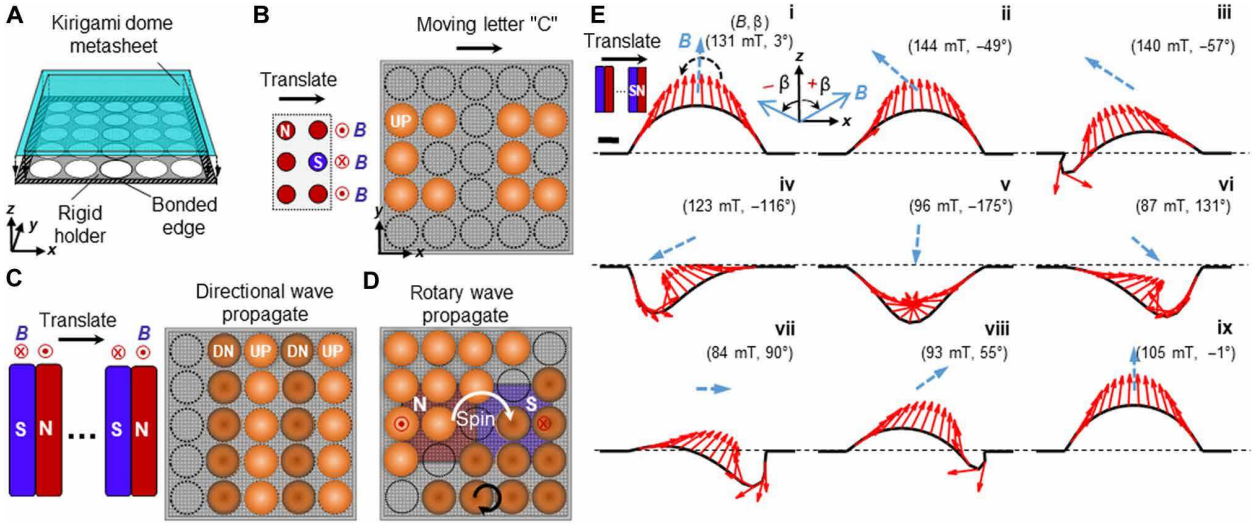

Fig. 3. Spatiotemporal dynamic shape-shifting in the magnetic kirigami dome metasheet. (**A**) Schematic of the shape-shifting metasheet platform with an attached rigid holder to eliminate the effect of pulling magnetic force and junction interaction between neighboring domes. (**B**) Schematic setup of an actuated moving letter C-like pattern in the metasheet when an array of localized patterned pillar magnets translates underneath. For clarity, the downward doming from the S-orientated magnet is not shown. (**C**) Schematic setup of an actuated directional wave (composed of upward and downward domes) propagation across the metasheet when an array of nine bar-shaped magnets with alternate orientations translate underneath. (**D**) Schematic setup of an actuated rotary wave (composed of upward and downward domes) propagation across the metasheet when a spinning capsule-shaped magnet rotates cw underneath. (**E**) Theoretical modeling results on the periodic dynamic shape-shifting in a single magnetic kirigami dome in response to a right-moving magnetic field (nine bar-shaped magnets with alternate orientations translate underneath). Translating the magnets changes both the magnitude (*B*) and direction (β) of the magnetic field. Scale bar, 1.5 mm.

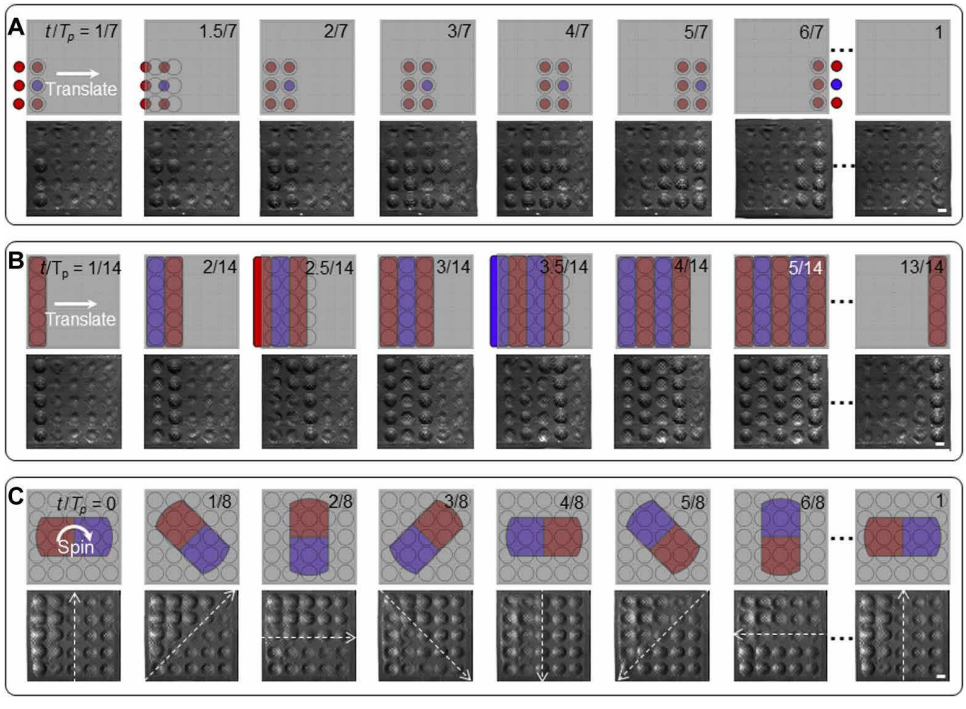

Fig. 4. Dynamic shape-shifting processes in the magnetic kirigami dome metasheet over one time period T_p in response to moving and rotating magnets underneath. (**A** to **C**) Time-lapse top-view schematics (top) and photos (bottom) of its shape-shifting processes under the actuation of an array of right-moving pillar (A) and bar-shaped (B) magnets and a cw-rotating capsule-shaped magnet (C). T_p = 0.4 s (A), 0.7 s (B), and 18.7 ms (C). The white arrows in (C) denote the rotational axis. Scale bars, 5 mm.

popping up or down the columns of domes (Fig. 4B), responding to the dynamically changing $\boldsymbol{B}$. Alternatively, Fig. 4C shows that, under a spinning magnetic field, the metasheet generates a rotational wave propagating around the rotational axis (white arrow). The rotational axis divides the metasheet into two symmetric halves with opposite doming directions and resides in the convex-to-concave transition region. The symmetric shape-shifting doming morphology transitions from a rectangular to triangular pattern, e.g., from the left pop-up rectangular region at $t = 0$ to the upper left and lower right pop-up triangle regions at $t = T_p/8$ and $5T_p/8T_p$, respectively, shown in Fig. 4C. The metasheet shows the same instantaneous wave-spinning speed and direction as the rotating magnet without lag, even at a high spinning speed of 1600 rpm, due to the fast response of the ferromagnetic elastomer (*28*). Theoretically, we find that the kirigami film in this work is highly responsive to cyclical magnetic actuation on the millisecond scale, with a response time of ~2 ms, suggesting that actuation at frequencies up to 250 Hz is possible (see the Supplementary Materials for more details).

Application: Multimodal and high-strength magnetic manipulation of nonmagnetic objects without grasping

Leveraging both the magnetic stiffening and propagating wave–like shape-shifting in the metasheet, we explore its applications as a multimodal remote object manipulation platform via dynamic adaptive interaction between the shape-shifting metasheet and objects without grasping.

Generally, manipulation of objects can be divided into grasping or nongrasping approaches. Grasping, such as pick-and-place, involves no relative motion between objects and manipulators via form or force closure, requiring grasping and retaining the objects (*29*). Nongrasping involves propelling or pushing without grasping to move an object, which is an important alternative when grasping is challenging, such as in handling fragile objects or in confined spaces (*30*).

Among the different actuation methods for manipulators, magnetic actuation is attractive for noncontact dexterous object manipulation due to its remote controllability and fast response (*31*–*33*). However, magnetically manipulating nonconductive and nonmagnetic objects is nontrivial (*34*). One way is to add ferromagnetic particles or skins to make the objects magnetically responsive (*31*) or to use magnetic grippers to grasp around the objects (*27*, *35*). The former requires additional steps to remove the magnetic additives, and the latter remains challenging to simultaneously control object grasping, retention, and transportation. A promising alternative is to use magnetically responsive surfaces to transport objects without grasping (*36*–*38*). However, such magnetic surfaces are mainly designed at small scales to manipulate microdroplets with negligible gravity (*36*, *37*), which shows limited load-bearing and transport capabilities in manipulating large-size droplets or beads when gravity becomes dominant (*38*). Using magnetic surfaces for nongrasping multimodal manipulation of nonconductive and nonmagnetic objects of different materials, sizes, shapes, and weights remains challenging and largely unexplored (*34*–*36*).

Using the localized C-shaped patterned magnets in Fig. 3B, we first explore the application of the shape-shifting kirigami dome metasheet as a stationary conveyor for multimodal nongrasping manipulation of both nonmagnetic solid beads (radius: 3.75 mm, ~20 mg) and water droplets (~50 μl), as shown in Fig. 5 (A to C) and Fig. 5 (D to H), respectively. For manipulation of water droplets, the metasheet is coated with a thin layer of superhydrophobic coating (Fig. 5, D and E; see Materials and Methods for details). When no magnetic field is applied, the small bead and water droplet can deform the planar metasheet and become lightly confined inside the concave dome under their self-weight due to the extreme compliance and flexibility of the metasheet. When the bead or droplet is placed in the center of the static localized C-shaped patterned magnetic field (i.e., on top of the blue-colored magnetic pillar), it becomes further trapped in a well due to the magnetically actuated downward doming in the center and the upward doming in its surroundings. When the patterned magnets move toward the center horizontally or vertically, the central dome switches from up to down, and the surrounding domes remain domed up. Consequently, the object confined by the C-shaped dome-up pattern has only one in-plane degree of freedom, resulting in its forward motion to next domed-down spot along the path in the array. The bead and droplet can be manipulated horizontally or vertically to the desired location, allowing multipath manipulation (Fig. 5, A, B, D, F, and G, and movie S6). In contrast, the continuous dome metasheet without cut fails to move the small bead. This is due to its shallow dome height and reduced load-lifting force under magnetic actuation. These limitations notably restrict the working space, preventing large degrees of shape morphing and effective object manipulation (movie S7). Furthermore, these mechanisms also allow the manipulation of multiple beads or water droplets individually or simultaneously. Figure 5G shows the merging of two different colored water droplets into one colored large droplet by individually moving each droplet. Figure 5 (C and H) demonstrates the simultaneous movement of two beads in parallel and six different sized droplets in two rows, respectively. This is achieved by using an extended array of the C-shaped patterned magnets (inset of Fig. 5, C and H). The six droplets in two rows merge into two large droplets in parallel after two sequential merging along the path.

Next, we explore applications of the dynamic shape-shifting kirigami metasheet for remote manipulation of nonconductive and nonmagnetic objects of different shapes, materials, and weights. Figure 6A shows the time-lapse images of linear transporting a lightweight rectangular wood plate (48 mm by 20 mm by 2 mm, 0.5 g) on top during one period ($T_p = 0.56$ s) of linear motion of an array of 12 bar-shaped magnets with alternate orientations. The wood plate covers nearly 3 by 2 (length × width) arrays of domes in the 5 by 5 metasheet. As the array of magnets moves to the left, the wood plate moves in the opposite direction to the right. Reversing the magnets' moving direction also reverses the object transportation direction. Thus, the metasheet enables bidirectional linear transportation of objects. This is due to the active interaction-induced thrust force between the propagating wave–like shape-shifting motion in the metasheet and the object on top. As the magnets move to the left, the dynamically changing localized magnetic field rotates cw, as marked by the red arrow in Fig. 6A, which drives the array of domes underneath the plate to asymmetrically and sequentially dome toward and propagate to the right by following the rotating magnetic field as discussed in Fig. 3E. Consequently, the asymmetric dynamic shape-shifting doming generates a cw torque to propel the plate backward (see the insets of Fig. 6A on the magnified photos of the shape changes in the dome), opposite to the moving direction of the magnets. In one period of linear motion of the magnets ($T_p = 0.56$ s), the metasheet moves the wood plate by 4.3 mm, which gives a transportation speed of 7.6 mm/s. Similarly,

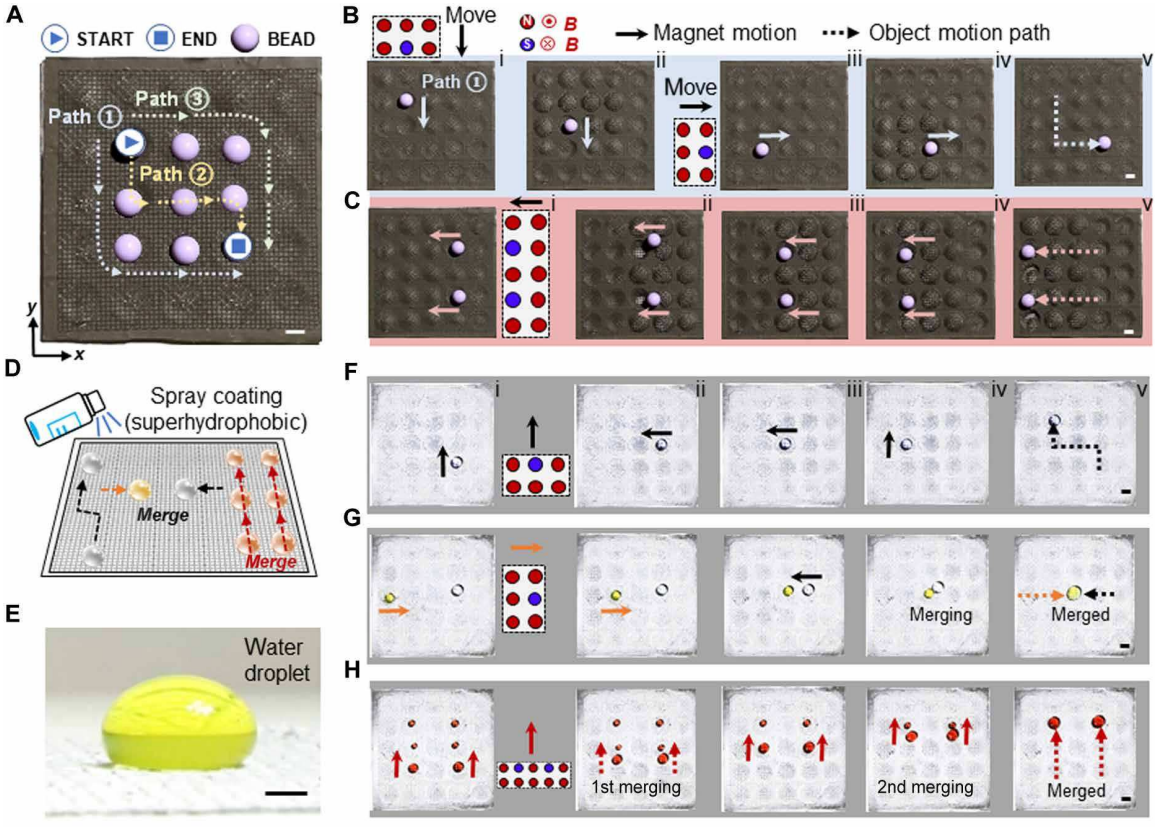

Fig. 5. Applications of the metasheet for remote magnetic multimodal manipulation of nonmagnetic solid beads and water droplets without grasping. (**A**) Schematic of multipath manipulation of plastic beads under an array of patterned C-shaped pillar magnets translating underneath. Scale bar, 5 mm. (**B**) Time-lapse top-view photos on the process of transporting the plastic bead from top left to bottom down following the predefined "L"-shaped pathway. Scale bar, 5 mm. (**C**) Time-lapse top-view photos on the process of simultaneously transporting two beads on the metasheet under an extended array of patterned pillar magnets, as schematically shown in the inset. Scale bar, 5 mm. (**D**) Schematics of the multimodal manipulation of single and multiple droplets on the superhydrophobic coated metasheet. (**E**) Front-view photo of a 50 μl-water droplet dyed with yellow color sitting on the superhydrophobic coated metasheet without penetration. Scale bar, 2 mm. (**F**) Time-lapse top-view photos on the process of transporting the water droplet (~50 μl) from bottom down to top left following the predefined zigzag pathway. Scale bar, 5 mm. (**G**) Time-lapse top-view photos on the process of merging two different colored water droplets (~30 μl for the yellow-colored droplet and ~50 μl for the light blue-colored droplet) into one large droplet by separate remote manipulation. Scale bar, 5 mm. (**H**) Time-lapse top-view photos on the process of simultaneously transporting and merging two parallel arrays of three aligned different sized red-colored droplets on the metasheet under an extended array of patterned pillar magnets. The two large droplets (~50 μl) sequentially merge and collect with small droplets (10 to 20 μl) along the desired pathways. Scale bar, 5 mm.

it can also transport other shapes of wooden plates in a reverse moving direction to the magnets, such as a star (Fig. 6B), triangle, pentagon, and irregular shapes that only cover a few domes, as well as simultaneously transport multiple different-shaped objects and ascend a small slope (9°) with a wood plate of ~1 g (fig. S10 and movie S8). Furthermore, it can also transport other representative nonmagnetic objects such as a slightly heavy glass slide (4.6 g; Fig. 6C) and an oversize leaf (Fig. 6D), as well as 3D objects with small area contact such as a saddle-shaped chip propelled only by two boundary line contacts (Fig. 6E). On the basis of the magnetic stiffening effect, it also shows high load-lifting and transportation capabilities of heavy objects that weigh 53.8 g, which is 35 times the self-weight of the metasheet (Fig. 6F). However, the average transportation speed is markedly reduced with increasing load (Fig. 6G). In contrast, the continuous dome metasheet fails to transport even lightweight objects, such as a small pentagonal wooden plate and an empty petri dish, which have small and large coverage areas, respectively (movie S9). Both objects remain stationary under the actuation of moving magnets. This emphasizes the advantages of magnetic kirigami designs over noncut continuous structures as the kirigami design enhances deformability while maintaining high stiffness. These qualities enable a larger working space for versatile shape morphing and provide superior load-bearing and load-lifting capabilities, allowing for various nongrasping object manipulation tasks.

Last, in addition to linear transportation, we demonstrate multimodal object manipulation in rotational motion driven by the spinning magnet (Fig. 7A and movie S10). When placing an object such as a petri dish (6.8 g) on the shape-shifting metasheet driven by a magnet spinning cw quickly, the dish starts to spin ccw slowly, opposite to the spinning direction of the magnet (see the arrows in Fig. 7B). The dish can still spin ccw when its weight becomes nearly doubled but with a much slower spinning speed (Fig. 7C). The object spinning speed ω_o has a nonlinear curve with the spinning rate of the magnet ω_m, where ω_o increases markedly with ω_m at a higher spinning rate over 1000 rpm (Fig. 7A). When $\omega_m = 1600$ rpm, ω_o is

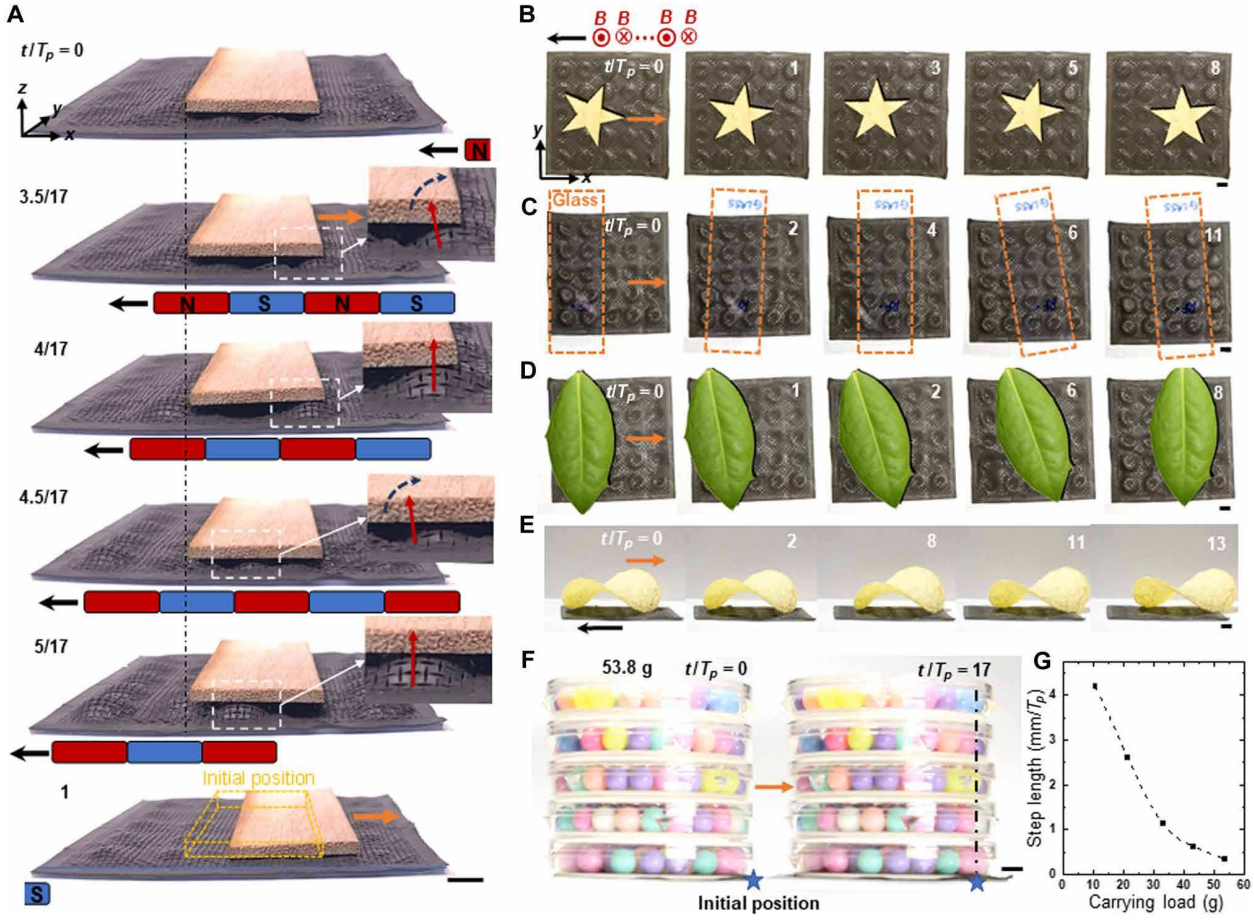

Fig. 6. Applications of the metasheet for remote magnetic multimodal manipulation of various nonmagnetic solid objects without grasping. (**A**) Time-lapse photos on the process of directionally transporting a lightweight rectangular wood plate (48 mm by 20 mm by 2 mm, 0.5 g) on the metasheet from left to right during one period (T_p = 3.18 s) under an array of 12 bar-shaped magnets with alternate orientations moving to the left. Scale bar, 5 mm. (**B** to **E**) Time-lapse top-view photos on the process of directionally transporting nonmagnetic objects of different shapes, materials, and sizes, including a star-shape wood plate (B), a glass slide (C), a large-size leaf (D), and a 3D potato chip (E) moving from left to right on the metasheet. Scale bars, 5 mm. (**F**) Illustration of lifting and transporting a heavy object, a stack of five petri dishes filled with plastic beads (53.8 g) on the metasheet (1.5 g). Scale bar, 5 mm. (**G**) Relationship between the average step length (moved distance in one time period) and the carrying loads of dish-shaped objects.

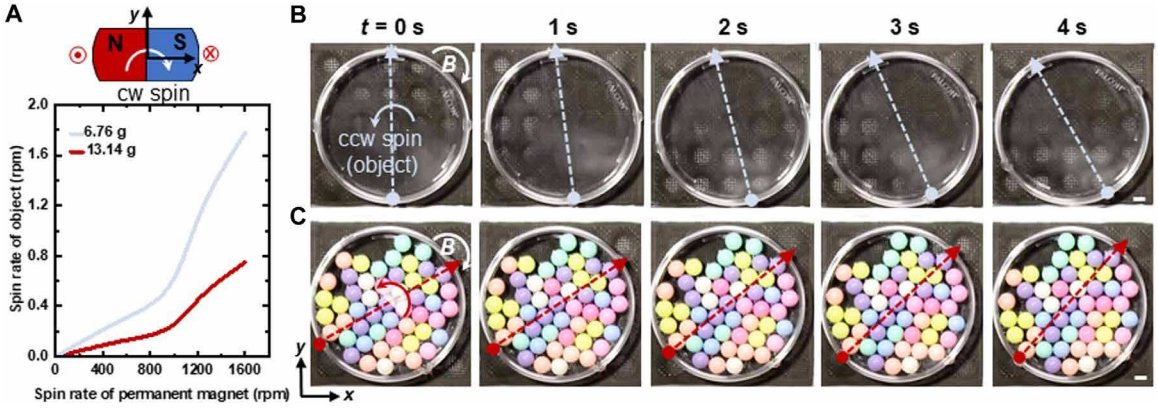

Fig. 7. Applications of the metasheet for remote magnetic rotational manipulation of nonmagnetic objects without grasping driven by the spinning magnet. (**A**) Top: Schematic of cw spinning of the capsule-shaped magnet. Bottom: Actuated spin rate of the dish-shaped objects with different weights as a function of the spin rate of the driving capsule-shaped magnet. (**B** and **C**) Time-lapse top-view photos on the actuated ccw rotating motions of an empty petri dish (6.8 g) and a filled petri dish with plastic beads (13.4 g) on the metasheet under the cw spinning of the capsule-shaped permanent (1000 rpm). Scale bars, 5 mm.

~1.8 and 0.8 rpm for the dish with and without extra loading weight, respectively, which are notably slower than the driving spinning rate. Similar to linear transportation, the inverse spinning motion in the object is due to the dynamically changing ccw rotating magnetic field along the tangential direction generated by the cw spinning magnet. Consequently, it generates a tangential torque to drive the ccw spinning of the object via the asymmetric dynamic shape-shifting doming along the tangential direction.

DISCUSSION

In this work, we combine inflatable soft kirigami domes with magnetic actuation to achieve both high deformability and high stiffness. The kirigami cuts drastically reduce the modulus while maintaining structural integrity, allowing adaptive dynamic shape morphing and providing a large working space for potential functionalities. The notable stiffening effect, induced by the interaction between the kirigami structures and external magnetic fields, enables high load-bearing and load-lifting capabilities. This combination of benefits showcases a potential application in remote magnetic multimodal nongrasping object transport, where both large morphing flexibility and high force outputs are required for effective manipulation.

Given the intriguing potential of inflatable kirigami structures for versatile shape morphing (*39*) and the fast remote actuation capabilities of magnetoresponsive elastomers (*13*–*15*), we envision that the concept of combining inflatable kirigami structures with magnetic elastomers could lead to the development of a broad range of soft shape-shifting structures with both high deformability and stiffness. These shape-morphing magnetic kirigami structures could have broad applications, including flexible mechanical metamaterials (*40*), shape-morphing matter (*4*), reconfigurable soft robots (*7*), nonprehensile robotic manipulation in confined and unstructured environments (*30*), biofluid droplet manipulation for biomedicine and medical diagnostics (*36*), and active haptic devices for displays and virtual reality (*41*).

Even compared to previous soft-hard and rigid platforms for shape morphing and object manipulation, such as the composite lattice-based robotic surface (*8*) and the rigid inFORM dynamic shape-shifting platform (*42*), our entirely soft magnetic kirigami platform stands out with unique advantages. First, our platform uses the adaptive interactions between the remote magnetic field and kirigami dome structures to substantially enhance and modulate stiffness in soft materials and structures. This stiffening effect enables high load-bearing, load-lifting, and transport capabilities, which are distinct from the inherently stiff components of soft composites (*8*) and rigid systems (*42*) that enable high stiffness for load-bearing. Second, our platform allows for both shape morphing and object manipulation through remote actuation, offering greater flexibility, simplified control, and autonomy. The composite robotic surface and inFORM platform required tethered systems with individual control over tens of LCE strip segments (*8*) or hundreds of motorized pins (*42*) to achieve complex dynamic shape changes. In contrast, our system autonomously adapts to moving magnets, simplifying both actuation and control for multimodal object manipulation.

Despite the promising results, several limitations remain. First, the rotation, bending, and stretching deformation of the discretely connected cut panels during inflation affect both magnetization and actuation, which are challenging to capture in the simplified 1D strip model. Full 3D continuum mechanics modeling and simulation are necessary to account for the intricate interactions between the 3D magnetized kirigami dome and external magnetic fields. Second, the underlying mechanism behind the optimal design for achieving both high deformability and stiffness has yet to be fully explored. Future 3D modeling will help uncover the physics behind the optimal design. Third, the versatility and accuracy of dynamic shape-shifting and object manipulation in the magnetic kirigami dome metasheet need further improvement.

MATERIALS AND METHODS

Fabrication of the magnetoresponsive kirigami metasheet

The base material of the magnetic metasheet was prepared by blending the uncured Ecoflex 00-50 (Smooth-On Inc., Part A and Part B were mixed with a weight ratio of 1:1) and neodymium-iron-boron (NdFeB) magnetic microparticles (MQFP-15-7-20065-089, Magnequench) with an average particle diameter of with the loading ratio of 60 wt % to Ecoflex 00-50. The uncured elastomer and NdFeB particles were well mixed and degassed for 10 min. The well-mixed composite was weighted to 4.19 g and spin coated on a petri dish with the dimension of 100 mm by 50 mm (EZ4, Schwan Technology, spin rate: 1500 rpm, 20 s). The petri dish was placed onto a hot plate (GUARDIAN 5000) at 55°C for 30 min. The cured material was cut to designed kirigami patterns using a laser cutter (EPILOG LASER 40 W). The remanent magnetization profiles of the magnetically programmed kirigami domes and array were characterized by measuring the magnetic fields in the out-of-plane direction across sample surfaces via a magneto-optical sensor (cmos-magview, Matesy, Jena, Germany). The samples are measured at the flattened disk shape under no external magnetic fields applied.

Inflation-induced magnetization of the magnetoresponsive metasheet

The pneumatic elastomeric inflators without encapsulation were fabricated following the conventional molding-demolding manufacturing strategy for fluid-driven soft actuators. The elastomeric inflators were encapsulated by Sil-Poxy (Smooth-On Inc.). The rigid holder was 3D printed using an Objet260 Connex3 (Stratasys Inc.) and assembled with the metasheet and the elastomeric inflator. The pressurized setup was placed between the poles of a GMW 3472-70 electromagnet for magnetization. The out-of-plane direction of the kirigami elastomer was parallel to two poles. Pressure $P = 33$ kPa was applied to inflate the kirigami elastomer. The uniform magnetizing fields with different intensities (1.03, 1.23, and 1.41 T) were applied. Removing pressure P and the magnetic field, the kirigami elastomer recovered to the flattened shape.

Indentation test under the magnetic field

The rigid holder with the hollow hole and the plastic indenter were 3D printed using an Objet260 Connex3 (Stratasys Inc.). The holder was clamped onto the frame of the mechanical tensile tester Instron 5944. The indenter was assembled with the loading cell (maximum range: 5 N). The metasheet, cylindrical permanent magnet (19 mm in diameter and 12.5 mm in thickness, N52), and rigid holder were aligned coaxially. The hemispherical indentation tip vertically indented the sample under a displacement control with a loading rate of 0.5 mm/min.

Capturing the deformation of the single magnetic kirigami dome under the uniform magnetic fields with varied inclined angle

The single magnetic dome was bonded with a rigid ring and placed between the poles of the electromagnets (GMW 3472-70). The digital camera (Canon 6D Mark II) assembled with a macro lens (Canon, EF 180 mm) was used to capture its deformation.

Assemblies, linear translation, and spinning rotation of the permanent magnet array

The bar-shaped permanent magnet array: 9 and 12 permanent bar-shaped magnets (MKD60103-6P, 60 mm by 10 mm by 3 mm in dimension, N45) aligned horizontally with alternative directions of magnetic poles to form an array. The array was fixed on a customized plastic holder. The pillar-shaped magnet array: multiple pillar-shaped permanent magnets (diameter of 6.3 mm and height of 25 mm, N52) inserted into a customized plastic holder as shown in fig. S11. Linear motion of the magnets: A prototype system was built to achieve the linear movement of the magnets. The magnets were mounted on a linear stage (FUYU FSL30 Mini Linear Stage), which is actuated by a stepper motor (NEMA 14). The motion system was controlled by a stepper driver (STEPPERONLINE, DM542T). The tunable spinning motion of the capsule-shaped permanent magnet was generated by a stir plate (VWR, 190205003).

High-speed motion capture

The evolving shape-shifting of the metasheet was captured by a high-speed camera (Photron SA-2) with the frame rate from 1500 to 8000 fps.

Experiment of water droplet manipulation

The magnetic metasheet was spray coated using commercial silica-based particles (NeverWet, RUST-OLEUM). The weight added after spray coating is ~0.5 g. The water droplets were dyed using colored resin (Microclekoo) without apparent variation of the surface tension.

Supplementary Materials

The PDF file includes:
Supplementary Text
Figs. S1 to S12
Table S1
Legends for movies S1 to S10

Other Supplementary Material for this manuscript includes the following:
Movies S1 to S10

REFERENCES AND NOTES

1. S. Li, K. W. Wang, Plant-inspired adaptive structures and materials for morphing and actuation: A review. *Bioinspir. Biomim.* **12**, 011001 (2016).
2. K. Oliver, A. Seddon, R. S. Trask, Morphing in nature and beyond: A review of natural and synthetic shape-changing materials and mechanisms. *J. Mater. Sci.* **51**, 10663–10689 (2016).
3. S.-J. Jeon, A. W. Hauser, R. C. Hayward, Shape-morphing materials from stimuli-responsive hydrogel hybrids. *Acc. Chem. Res.* **50**, 161–169 (2017).
4. X. Yang, Y. Zhou, H. Zhao, W. Huang, Y. Wang, K. J. Hsia, M. Liu, Morphing matter: From mechanical principles to robotic applications. *Soft Sci.* **3**, 38 (2023).
5. D. Jiao, Q. L. Zhu, C. Y. Li, Q. Zheng, Z. L. Wu, Programmable morphing hydrogels for soft actuators and robots: From structure designs to active functions. *Acc. Chem. Res.* **55**, 1533–1545 (2022).
6. D. Hwang, E. J. Barron, A. B. M. T. Haque, M. D. Bartlett, Shape morphing mechanical metamaterials through reversible plasticity. *Sci. Robot.* **7**, eabg2171 (2022).
7. J. Sun, E. Lerner, B. Tighe, C. Middlemist, J. Zhao, Embedded shape morphing for morphologically adaptive robots. *Nat. Commun.* **14**, 6023 (2023).
8. K. Liu, F. Hacker, C. Daraio, Robotic surfaces with reversible, spatiotemporal control for shape morphing and object manipulation. *Sci. Robot.* **6**, eabf5116 (2021).
9. T. van Manen, S. Janbaz, A. A. Zadpoor, Programming the shape-shifting of flat soft matter. *Mater. Today* **21**, 144–163 (2018).
10. S. J. P. Callens, A. A. Zadpoor, From flat sheets to curved geometries: Origami and kirigami approaches. *Mater. Today* **21**, 241–264 (2018).
11. G. P. T. Choi, L. H. Dudte, L. Mahadevan, Programming shape using kirigami tessellations. *Nat. Mater.* **18**, 999–1004 (2019).
12. Y. Hong, Y. Chi, S. Wu, Y. Li, Y. Zhu, J. Yin, Boundary curvature guided programmable shape-morphing kirigami sheets. *Nat. Commun.* **13**, 530 (2022).
13. Y. Bai, H. Wang, Y. Xue, Y. Pan, J.-T. Kim, X. Ni, T.-L. Liu, Y. Yang, M. Han, Y. Huang, J. A. Rogers, X. Ni, A dynamically reprogrammable surface with self-evolving shape morphing. *Nature* **609**, 701–708 (2022).
14. Y. Alapan, A. C. Karacakol, S. N. Guzelhan, I. Isik, M. Sitti, Reprogrammable shape morphing of magnetic soft machines. *Sci. Adv.* **6**, eabc6414 (2020).
15. G. Z. Lum, Z. Ye, X. Dong, H. Marvi, O. Erin, W. Hu, M. Sitti, Shape-programmable magnetic soft matter. *Proc. Natl. Acad. Sci. U.S.A.* **113**, E6007–E6015 (2016).
16. H. Zhu, Y. Wang, Y. Ge, Y. Zhao, C. Jiang, Kirigami-inspired programmable soft magnetoresponsive actuators with versatile morphing modes. *Adv. Sci.* **9**, e2203711 (2022).
17. L. Wang, Y. Chang, S. Wu, R. R. Zhao, W. Chen, Physics-aware differentiable design of magnetically actuated kirigami for shape morphing. *Nat. Commun.* **14**, 8516 (2023).
18. L. T. Gaeta, K. J. McDonald, L. Kinnicutt, M. Le, S. Wilkinson-Flicker, Y. Jiang, T. Atakuru, E. Samur, T. Ranzani, Magnetically induced stiffening for soft robotics. *Soft Matter* **19**, 2623–2636 (2023).
19. P. Duhr, Y. A. Meier, A. Damanpack, J. Carpenter, A. R. Studart, A. Rafsanjani, A. F. Demirörs, Kirigami makes a soft magnetic sheet crawl. *Adv. Sci.* **10**, e2301895 (2023).
20. Y. Cho, J.-H. Shin, A. Costa, T. A. Kim, V. Kunin, J. Li, S. Y. Lee, S. Yang, H. N. Han, I.-S. Choi, D. J. Srolovitz, Engineering the shape and structure of materials by fractal cut. *Proc. Natl. Acad. Sci. U.S.A.* **111**, 17390–17395 (2014).
21. Y. Tang, G. Lin, L. Han, S. Qiu, S. Yang, J. Yin, Design of hierarchically cut hinges for highly stretchable and reconfigurable metamaterials with enhanced strength. *Adv. Mater.* **27**, 7181–7190 (2015).
22. Y. Tang, J. Yin, Design of cut unit geometry in hierarchical kirigami-based auxetic metamaterials for high stretchability and compressibility. *Extreme Mech. Lett.* **12**, 77–85 (2017).
23. A. Brinkmeyer, M. Santer, A. Pirrera, P. M. Weaver, Pseudo-bistable self-actuated domes for morphing applications. *Int. J. Solids Struct.* **49**, 1077–1087 (2012).
24. J. A. Faber, J. P. Udani, K. S. Riley, A. R. Studart, A. F. Arrieta, Dome-patterned metamaterial sheets. *Adv. Sci.* **7**, 2001955 (2020).
25. A. Rafsanjani, K. Bertoldi, Buckling-induced kirigami. *Phys. Rev. Lett.* **118**, 084301 (2017).
26. J. Yin, M. Retsch, J.-H. Lee, E. L. Thomas, M. C. Boyce, Mechanics of nanoindentation on a monolayer of colloidal hollow nanoparticles. *Langmuir* **27**, 10492–10500 (2011).
27. J. A.-C. Liu, J. H. Gillen, S. R. Mishra, E. E. Evans, J. B. Tracy, Photothermally and magnetically controlled reconfiguration of polymer composites for soft robotics. *Sci. Adv.* **5**, eaaw2897 (2019).
28. Y. Kim, H. Yuk, R. Zhao, S. A. Chester, X. Zhao, Printing ferromagnetic domains for untethered fast-transforming soft materials. *Nature* **558**, 274–279 (2018).
29. A. Billard, D. Kragic, Trends and challenges in robot manipulation. *Science* **364**, eaat8414 (2019).
30. M. T. Mason, Progress in nonprehensile manipulation. *Int. J. Rob. Res.* **18**, 1129–1141 (1999).
31. Y. Kim, X. Zhao, Magnetic soft materials and robots. *Chem. Rev.* **122**, 5317–5364 (2022).
32. Z. Yang, L. Zhang, Magnetic actuation systems for miniature robots: A review. *Adv. Intell. Syst.* **2**, 2000082 (2020).
33. J. J. Abbott, E. Diller, A. J. Petruska, Magnetic methods in robotics. *Annu. Rev. Control Robot. Auton. Syst.* **3**, 57–90 (2020).
34. L. N. Pham, G. F. Tabor, A. Pourkand, J. L. Aman, T. Hermans, J. J. Abbott, Dexterous magnetic manipulation of conductive non-magnetic objects. *Nature* **598**, 439–443 (2021).
35. Q. Ze, X. Kuang, S. Wu, J. Wong, S. M. Montgomery, R. Zhang, J. M. Kovitz, F. Yang, H. J. Qi, R. Zhao, Magnetic shape memory polymers with integrated multifunctional shape manipulation. *Adv. Mater.* **32**, e1906657 (2020).
36. Y. Zhou, S. Huang, X. Tian, Magnetoresponsive surfaces for manipulation of nonmagnetic liquids: Design and applications. *Adv. Funct. Mater.* **30**, 1906507 (2020).
37. K. Ni, Z. Wang, Recent progress on the development of magnetically-responsive micropillars: Actuation, fabrication, and applications. *Adv. Funct. Mater.* **33**, 2213350 (2023).
38. S. Jiang, D. Wu, J. Li, J. Chu, Y. Hu, Magnetically responsive manipulation of droplets and bubbles. *Droplet* **3**, e117 (2024).

39. L. Jin, A. E. Forte, B. Deng, A. Rafsanjani, K. Bertoldi, Kirigami-inspired inflatables with programmable shapes. *Adv. Mater.* **32**, e2001863 (2020).
40. K. Bertoldi, V. Vitelli, J. Christensen, M. Van Hecke, Flexible mechanical metamaterials. *Nat. Rev. Mater.* **2**, 1–11 (2017).
41. Y. Tang, J. Xu, Q. Liu, X. Hu, W. Xue, Z. Liu, Z. Lin, H. Lin, Y. Zhang, Z. Zhang, X. Ma, J. Wang, J. Zhong, D. Wang, H. Jiang, Y. Ma, Advancing haptic interfaces for immersive experiences in the metaverse. *Device* **2**, 100365 (2024).
42. S. Follmer, D. Leithinger, A. Olwal, A. Hogge, H. Ishii, in *Proceedings of the 26th Annual ACM Symposium on User Interface Software and Technology* (ACM, 2013), vol. 13, pp. 417–426.

Acknowledgments: We thank A. Kota and S. Vallabhuneni for assistance with motion capture using the high-speed camera and D. Makarov's lab for assistance with measuring the magnetization profile of the magnetic kirigami metasheet. We acknowledge use of the MPMS in the Department of Materials Science and Engineering at North Carolina State University. **Funding:** J.Y. acknowledges the funding support from the NSF (CMMI-2005374 and CMMI-2329674). J.B.T. and E.E.E. acknowledge the funding support from the NSF (CMMI-1663416 and CMMI-1662641). This work was performed in part at the Analytical Instrumentation Facility (AIF) at North Carolina State University, which is supported by the State of North Carolina and the NSF (ECCS-2025064). The AIF is a member of the North Carolina Research Triangle Nanotechnology Network (RTNN), a site in the National Nanotechnology Coordinated Infrastructure (NNCI). **Author contributions:** Y.C., J.Y., and J.B.T. developed the concept and designed the experiments. J.Y. and J.B.T. supervised the project. Y.C. fabricated and characterized mechanical properties of prototypes. E.E.E. conducted the theoretical modeling and numerical simulation. M.R.C. and S.N.C. characterized magnetic properties. Y.C., F.Q., and H.S. characterized dynamic morphing and object manipulation of prototypes. Y.C. and C.M.C. conducted the finite element simulation. Y.C., J.Y., and E.E.E. wrote the manuscript. All authors contributed to the discussion, data analysis, and editing of the manuscript. **Competing interests:** The authors declare that they have no competing interests. **Data and materials availability:** All data needed to evaluate the conclusions in the paper are present in the paper and/or the Supplementary Materials.

Submitted 17 July 2024
Accepted 30 October 2024
Published 6 December 2024
10.1126/sciadv.adr8421